

Revealing the effect of crystallinity and oxygen vacancies of Fe-Co phosphate on oxygen evolution for high-current water splitting

Xinqiang Liu^{a,1}, Haoran Yin^{a,1}, Shifan Zhang^a, Menghan Huang^a, Tayirjan Taylor Isimjan^c,
Xiulin Yang^{a,*}, Dandan Cai^{a,b,*}

^a Guangxi Key Laboratory of Low Carbon Energy Materials, School of Chemistry and Pharmaceutical Sciences, Guangxi Normal University, Guilin 541004, China

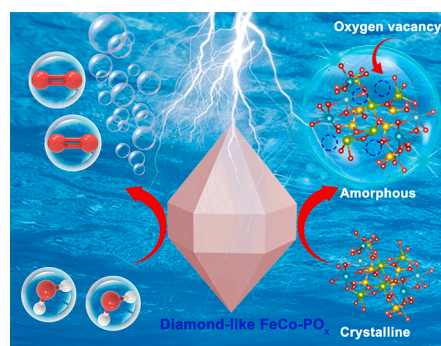
^b School of Chemical Engineering and Technology, Sun Yat-sen University, Zhuhai 519082, China

^c Saudi Arabia Basic Industries Corporation (SABIC), King Abdullah University of Science and Technology (KAUST), Thuwal 23955-6900, Saudi Arabia

HIGHLIGHTS

- An amorphous FeCo-PO_x is constructed by hydrothermal and phosphating treatments.
- The catalyst owns a diamond-like morphology and abundant oxygen vacancies.
- The catalyst exhibits excellent OER and overall water splitting activity and stability.
- The synergy of rich oxygen vacancy and amorphous structure are the key to improve performance.

GRAPHICAL ABSTRACT



ARTICLE INFO

Keywords:

Transition metal phosphates
Amorphous
Oxygen vacancy
Oxygen evolution
Overall water splitting

ABSTRACT

Strategically tuning the composition and structure of transition metal phosphates (TMPs) holds immense promise in the development of efficient oxygen evolution reaction (OER) electrocatalysts. However, the effect of crystalline phase transformation for TMPs on the catalytic OER activity remains relatively uncharted. In this study, we have deftly orchestrated the reaction process of anion-etched precursor to induce the amorphization process of FeCo-PO_x from crystalline to amorphous states. The as-obtained amorphous FeCo-PO_x (A-FeCo-PO_x) exhibited an optimized OER performance with a low overpotential of 270 mV at a current density of 10 mA cm⁻², which could be attributed to the flexibility of its amorphous structure and the synergistic effect of oxygen vacancies. Moreover, when incorporated into an overall water splitting (OWS) device configured as A-FeCo-PO_x(⁺)||Pt/C(⁻), it displayed long-term solid stability, sustaining operation for 300 h at a current density of 200 mA cm⁻². This work not only provides valuable insights into understanding the transformation from crystalline to amorphous states, but also establishes the groundwork for the practical utilization of amorphous nanomaterials in the field of water splitting.

* Corresponding authors.

E-mail addresses: xlyang@gxnu.edu.cn (X. Yang), caidandan86@163.com (D. Cai).

¹ These authors contribute equally to this work.

<https://doi.org/10.1016/j.jcis.2023.09.185>

Received 31 July 2023; Received in revised form 27 September 2023; Accepted 29 September 2023

Available online 1 October 2023

0021-9797/© 2023 Elsevier Inc. All rights reserved.

1. Introduction

The depletion of fossil fuels has created an urgent need for the development of green and sustainable alternative energy sources [1,2]. Currently, hydrogen energy is considered as a promising candidate to replace fossil fuels due to its high energy density and eco-friendliness [3]. Water splitting has great potential as an efficient energy storage and conversion technology for generating high-purity hydrogen energy [4]. However, electrochemical water splitting technology face challenges due to the slow kinetics resulting from inherent four-electron–proton coupling process of the anodic oxygen evolution reaction (OER) [5,6]. Although commercial OER catalysts such as RuO₂ and IrO₂ are commonly used, their scarcity and cost limit their large-scale application [7,8]. Consequently, it becomes essential to explore more efficient, cost-effective and non-precious metal-based alternatives to replace these precious metal-based catalysts [9–14].

Recently, non-precious metal-based electrocatalysts have been widely investigated for OER, such as transition metal phosphates [15], nitrides [16], oxides [17], hydroxides [18] and metal organic frameworks (MOFs) [19]. The phosphate groups (-PO_x) in transition metal phosphates not only act as proton acceptors to enhance the oxidation of metal atoms, but also cause distortion of the metal geometry, contributing to the adsorption of water and subsequent oxidation [20,21]. The use of hypophosphite (NaH₂PO₂) as a phosphorus source in vapor–solid phosphatization reactions maximizes the retention of the precursor morphology [22,23]. For example, Liu's group successfully synthesized core–shell Ni-Co@Fe PBA nanocubes using the lattice-matching principle and further transformed them into hollow Ni-Co-Fe-P nanoboxes by an interface-induced shrinkage process [24]. The hollow structure provided increased accessibility of active sites and improved electrolyte contact, resulting in a low overpotential of 277 mV at a current density of 20 mA cm⁻². Conventional strategies have focused on modifying the size, morphology, and structure of catalysts to enhance their electrocatalytic activity [25,26]. However, an alternative and valid approach to improve the exposed active sites and electrical conductivity of catalysts is by modifying the crystallinity through the transformation of catalyst composition [27,28]. This concept, though meaningful, has rarely been implemented in experiments.

From a catalytic point of view, amorphous catalysts have gained significant attention due to their enhanced flexibility in terms of structure and composition [29,30]. In contrast to conventional crystalline catalysts, the aperiodic arrangement and abundant randomly oriented bonds in the amorphous phase endow the catalysts with plentiful coordination-unsaturated active sites and vacancies compared to traditional crystalline counterparts [31,32]. Therefore, a large number of active sites facilitate the adsorption process and improve electrocatalytic performance [33]. Additionally, the structural flexibility of amorphous region allows the materials to self-regulate and withstand structural disturbances during electrocatalysis, leading to improve long-term stability [34,35]. Furthermore, short-range local structural disorder can promote intrinsic OER activity due to strong electron-lattice coupling effect [36,37]. For instance, Yu et al. demonstrated that the OER performance of amorphous NiFeMo oxides was better than that of crystalline counterparts in alkaline electrolytes [38]. Unfortunately, the strong and isotropic nature of metallic bonds usually results in the synthesis of crystalline metallic nanomaterials [39,40]. Therefore, it remains a substantial challenge to fundamentally understand the transition of metal nanomaterial from crystalline to amorphous state, while precisely controlling elemental composition, material size, and shape.

In this study, we have successfully induced the structural evolution of FeCo-PO_x from crystalline to amorphous state by intentionally modulating the reaction times during the anion-etching process of MOFs precursor. Transmission electron microscopy (TEM) results confirmed that the resulting samples retained the size and shapes of the MOFs precursor. The resulting long-range disordered architecture contained abundant oxygen vacancies and localized crystallinity, enabling the

sample to expose more available active sites and facilitating adsorption/desorption of OER intermediates. Thanks to this amorphous structure, the optimized amorphous FeCo-PO_x (A-FeCo-PO_x) electrode exhibited optimized OER performance and long-term stability. In addition, a low cell voltage of 1.54 V at 10 mA cm⁻² was obtained using an electrolyzer assembled with A-FeCo-PO_x and commercial Pt/C, which was slightly better than the benchmark RuO₂||Pt/C⁽⁻⁾ catalyst. In addition, the A-FeCo-PO_x||Pt/C⁽⁻⁾ device demonstrated long-term durability for 300 h of operation at 200 mA cm⁻². This work not only revealed the amorphous process, but also provided valuable insights into the design of highly active amorphous materials to replace noble metal-based OER catalysts.

2. Experimental section

2.1. Materials

All chemicals were analytical grade purity and were used without further purification. Iron (III) nitrate nonahydrate (Fe(NO₃)₃·9H₂O), Cobalt (II) nitrate hexahydrate (Co(NO₃)₂·6H₂O, 99%), Fumaric acid (95%), sodium hypophosphite monohydrate (NaH₂PO₂·H₂O) and potassium hydroxide (KOH) were bought from Aladdin Chemical Reagent Co. Ltd (Shanghai, China). RuCl₃·3H₂O (37%) was bought by Inno-chem Co. Ltd. Commercial Pt/C (20 wt% Pt, Sinerio, 1 g) was purchased from Alfa Aesar. Nafion solution (5 wt%) was purchased from DuPont Co. Ltd. N, N-dimethylformamide (DMF, 98%) and Dehydrated ethanol (EtOH, 99.7%) were supplied by Xilong Chemical Reagent Co. Ltd. Carbon Fiber Paper (CFP) was purchased from Toray Co. Ltd and was modified hydrothermally with 68% HNO₃ at 120 °C for 3 h in sequence to activate the surface of CFP, and then washing with deionized water to neutral and dried at room temperature.

2.2. Synthesis of diamond-like Fe-MIL-88A

Fe(NO₃)₃·9H₂O (0.5 mmol) and fumaric acid (8 mmol) were dissolved in the solution with 10 mL DMF. A well-dispersed solution was formed by vigorous ultrasonic dissolution and magnetic stirring. Afterward, the mixture was transferred to a 25 mL Teflon-lined stainless steel autoclave and reacted at 120 °C for 12 h. The powder was collected by centrifugation with ethanol/DMF for three times and dried at 30 °C overnight.

2.3. Synthesis of diamond-like FeCo-MIL-88A

Fumaric acid (8 mmol) was dissolved in the solution with 5 mL DMF by ultrasonic to form solution 1. Subsequently, Fe(NO₃)₃·9H₂O (0.5 mmol) and Co(NO₃)₂·9H₂O (0.25 mmol) were dissolved in 5 mL DMF to form solution 2. Solution 1 was poured into solution 2 and stirred for thirty minutes. And the remaining steps were the same as for the synthesis of Fe-MIL-88A.

2.4. Synthesis of diamond-like A-Fe-PO_x

The prepared diamond-like Fe-MIL-88A was etched by the thermal decomposition of NaH₂PO₂·H₂O under N₂ atmosphere. Two porcelain boats were loaded with 1.0 g NaH₂PO₂·H₂O and 50 mg diamond-like Fe-MIL-88A in the tubular furnace, respectively. Then the temperature of tube furnace was elevated to 300 °C and kept for 2 h under N₂. The black samples were obtained after natural cooling to ambient temperature under N₂ flow and denoted as A-Fe-PO_x.

2.5. Synthesis of diamond-like A-FeCo-PO_x

The similar procedure was adopted for the preparation of A-FeCo-PO_x, except replacing the precursor from Fe-MIL-88A to FeCo-MIL-88A. The preparation method of control samples was the same except that the

reaction time was shortened to 1.5, 1.0 and 0.5 h.

2.6. Structural characterization

The crystal structure of resultant products was analyzed by Rigaku D/Max-3c powder X-ray diffractometer (XRD) with Cu K α radiation. The morphologies of sample were identified by TEM (Talos F200S) and field-emission scanning electron microscopy (FESEM; Quanta 200 FEG), respectively. Energy-dispersive X-ray spectroscopy (EDX) was used to detect the elemental composition. Chemical states were gathered by X-ray photoelectron spectrometer (XPS; NEXSA). The groups of catalyst were characterized by Fourier-transform infrared spectroscopy (FT-IR; Spectrum Two) and Raman spectra collected by inVia Quotation Evolution. The metal ratio was performed by inductively coupled plasma-mass spectroscopy (ICP-MS; FLEXAR-NEXION300X). We performed multiple experiments using ICP-MS to reduce errors and ensure data accuracy and reproducibility. The electron paramagnetic resonance (EPR) was determined on the Endor spectrometer (Bruker A300). Thermal gravimetric analysis (TGA) was conducted via employing a TG203F3 tarsus thermal analyzer. The Brunauer-Emmett-Teller (BET) N₂ adsorption/desorption isotherms were explored utilizing a Micromeritics ASAP 2020 analyzer. The specific surface areas of the products were calculated by the Non Local Density Functional Theory (NLDFT) method based on the collected N₂ adsorption isotherms.

2.7. Electrochemical measurements

Electrochemical data was tested by CHI760E electrochemical workstation (Chenhua Instrument) with a standard three electrode system in 1.0 M KOH solution (pH = 13.6). In the system, CFP was used as the working electrode, while an Ag/AgCl and a carbon rod electrode utilizing as reference electrode and counter electrode, respectively. To prepare the working electrode, 2 mg sample was placed in a mixed solution with 125 μ L water, 125 μ L isopropanol and 25 μ L 5 wt% Nafion under ultrasonication for 30 min to form a homogeneous suspension,

and then previous suspension was dropped on the CFP electrode (loading area = 0.5 cm²).

To examine the electrocatalytic activity of the products, the linear sweep voltammetry (LSV) was recorded from 0.2 to 0.8 V (Ag/AgCl, 0.1989 V vs. RHE). All the polarization curves were corrected with 95% *i*R-compensation. All the parameters in this work were transformed to the reversible hydrogen electrode (RHE) according to the standard Nernst equation: $E_{RHE} = (E_{Ag/AgCl} + 0.059 \times \text{pH} + 0.1989)$ V. The corresponding Tafel slope was calculated from $\eta = b \log j + a$, where η is equal to the overpotential ($\eta = E_{RHE} - 1.23$ V), b represent the Tafel slope, and j is the current density. Electrochemical impedance spectroscopy (EIS) was performed in the frequency range of 10⁵ Hz to 10 Hz with an AC amplitude of 5 mV at a potential of 1.48 V (vs. RHE). The chronopotentiometry (CP) test to evaluate the stability were carried out at a constant current density of 10.0 mA cm⁻² without *i*R compensation.

A full electrolyzer configuration was assembled using A-FeCo-PO_x as the anode and commercial Pt/C as the cathode, and measurements were performed in a two-electrode cell with a carbon paper as the carrier in 1.0 M KOH solution. The catalyst suspension was dropped on the CFP by pipette (the catalyst loading is the same as the three-electrode cell).

3. Results and discussion

3.1. Structural and morphological characterizations

Fig. 1a illustrated the synthetic routes of FeCo-MIL-88A and A-FeCo-PO_x. Initially, the diamond-like FeCo-MIL-88A precursor was prepared through solvothermal reaction. Subsequently, the amorphous A-FeCo-PO_x of diamond-shaped was synthesized by anionic etching phosphatization in N₂ atmosphere using FeCo-MIL-88A as precursor. And the thermal stability of Fe-MIL-88A was examined by TGA (Fig. 1b).

The crystal structure of synthesized samples was examined by XRD. As depicted in Fig. 1c, the diffraction peaks of Fe-MIL-88A and FeCo-MIL-88A coincided with previously reported crystal data (Cambridge Crystallographic Data Centre, CCDC number: 644016), indicating the

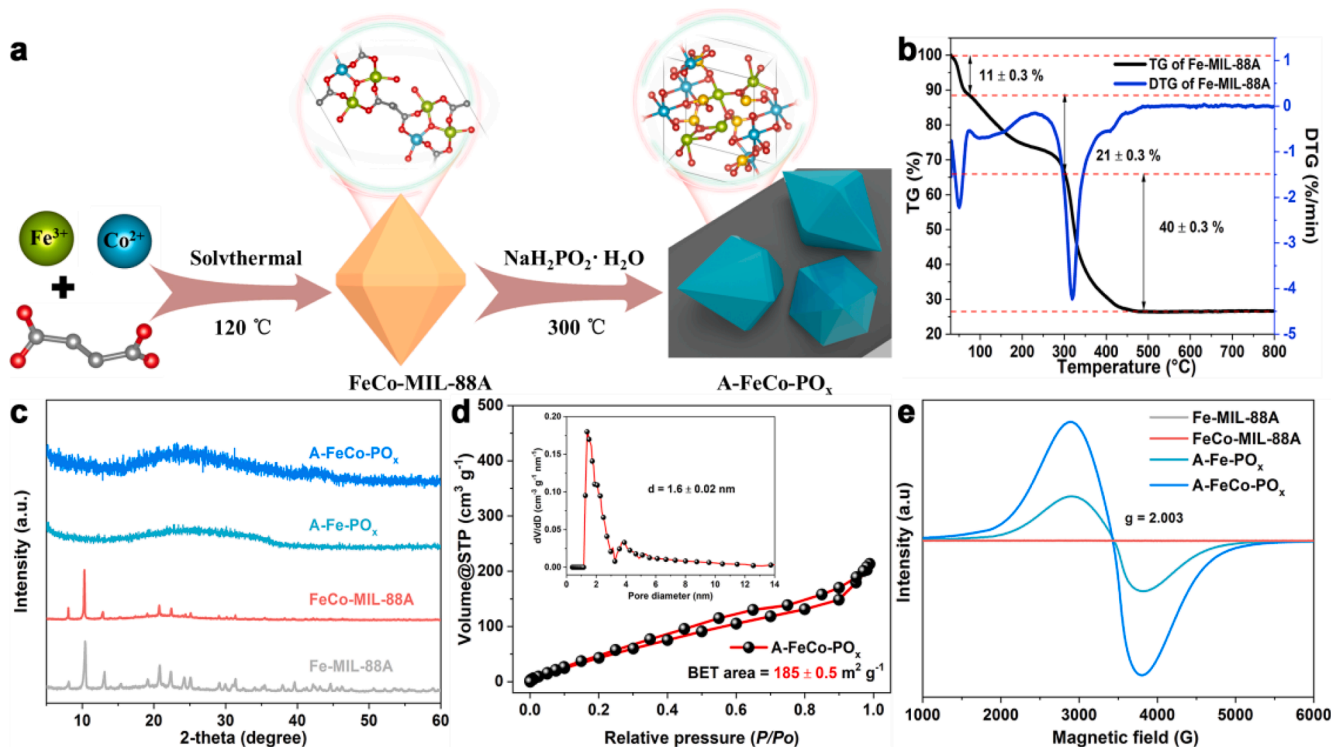


Fig. 1. (a) Scheme for the synthesis of A-FeCo-PO_x, (b) TG and DTG curves of Fe-MIL-88A, (c) XRD patterns of Fe-MIL-88A, FeCo-MIL-88A, A-Fe-PO_x and A-FeCo-PO_x, (d) N₂ adsorption–desorption isotherm of A-FeCo-PO_x (inset: corresponding pore size distribution curve), and (e) EPR spectra of FeCo-MIL-88A and A-FeCo-PO_x.

successful preparation of MIL-88A framework with good crystallinity [41]. However, the XRD pattern of A-Fe-PO_x and A-FeCo-PO_x after the anionic etching reaction signified typical amorphous features dominated by “broad peaks”. This phenomenon suggested a lack of long-range periodic order in the structure of A-Fe-PO_x and A-FeCo-PO_x, leading to the absence of Bragg peaks [40].

Fig. 1d illustrated a representative type IV N₂ adsorption–desorption isotherm in which micropores were predominantly present with a BET surface area of 185 m² g⁻¹ and an average pore size of about 1.5 nm. In contrast, the BET surface area of FeCo-MIL-88A was smaller at 145 m² g⁻¹ (Fig. S1). This comparison indicated that amorphous materials characterized by long-range disorder and short-range order structures could increase the specific surface area, maximizing the utilization of active site [42]. This effect was further investigated by EPR analysis, where A-Fe-PO_x and A-FeCo-PO_x exhibited the strong signals at *g* = 2.003, indicating the presence of unpaired electrons generated by oxygen vacancies at the metal sites (Fig. 1e) [43]. The bimetallic A-FeCo-PO_x showed a stronger signal compared to the monometallic A-Fe-PO_x, suggesting that the introduction of Co ions led to the formation of more vacancies [44].

The effect of anion source and etching time on the crystal structure of the products was further investigated. Fe-MIL-88A and FeCo-MIL-88A were calcined for 0.5 h and 2.0 h, respectively, without the addition of an anion source to obtain Fe-300 0.5 h, Fe-300 2.0 h, FeCo-300 0.5 h and FeCo-300 2.0 h. Figure S2 revealed that the diffraction peaks of FeCo-300 0.5 h and FeCo-300 2.0 h were consistent with the standard diffraction pattern of CoFe₂O₄ (JCPDS: 22–1086). These findings confirmed that the P sources were crucial for the formation of amorphous metal phosphates. Subsequently, the evolution of products structure was investigated for different etching time (0.5 h, 1.0 h, and 1.5 h) in Fig. 2a and 2b. The powder XRD data of Fe-PO_x 0.5 h and FeCo-PO_x 0.5 h was isostructural to the known crystal structure of iron phosphate, indicating that the samples were only partially reacted and remained in the crystalline state of iron phosphate [45]. The characteristic peaks of iron phosphate gradually became weaker as the extension of etching time. When the etching time was increased to 2 h,

the characteristic peaks of iron phosphate completely disappeared and transformed into an amorphous material. The bimetallic samples also exhibited similar results. Meanwhile, the variation of BET surface area during the transition from crystalline to amorphous state was also detected. As displayed in Fig. S3, the BET specific surface area of samples gradually increased from crystalline to amorphous form, which suggested that amorphous material with short-range ordered structure possessed the largest specific surface area [36].

FT-IR and Raman spectroscopy could be used to identify the presence of functional groups and infer short-range ordering structure. As shown in Fig. 2c, the adsorption peak located at nearly 1000 cm⁻¹ in the FT-IR spectrum could be assigned to the P—O peak of PO₄³⁻ unit [46]. This peak indicated the presence of phosphate groups in the amorphous material, which is consistent with the transformation from the crystalline Fe-MIL-88A or FeCo-MIL-88A precursor to amorphous A-FeCo-PO_x. Furthermore, Raman spectroscopy also depicted the characteristic peaks of phosphate groups, further confirming the presence of these groups in amorphous material (Fig. 2d) [47]. In this case, it was reasonable to assume that amorphous materials retained the basic building blocks and connectivity of their crystalline counterparts, even though they lacked any long-range periodic order [40]. The atomic arrangement of crystal structure and amorphous structure was shown in Fig. 2e and Fig. 2f.

The morphology and size of obtained samples were characterized by TEM images. As presented in Fig. 3a and Fig. S4, both A-Fe-PO_x and A-FeCo-PO_x exhibited diamond-like morphology and retained the morphology of their MOFs precursor (Fig. S5 and S6). The high-resolution TEM (HR-TEM) analysis in Fig. 3b revealed the absence of lattice fringes in the obtained amorphous materials [48]. This observation, along with the absence of Bragg peaks (Fig. 3c) and selected-area electron diffraction (SAED) analysis (Fig. 3d), provided evidence for the formation of amorphous metal phosphates [39]. These results were in agreement with XRD pattern. EDX mapping spectra confirmed the uniform spatial distribution of Fe, Co, O, and P elements in A-FeCo-PO_x (Fig. 3e). The elemental contents were further quantified using ICP-MS (Table S1).

XPS was conducted to probe the surface chemical states and

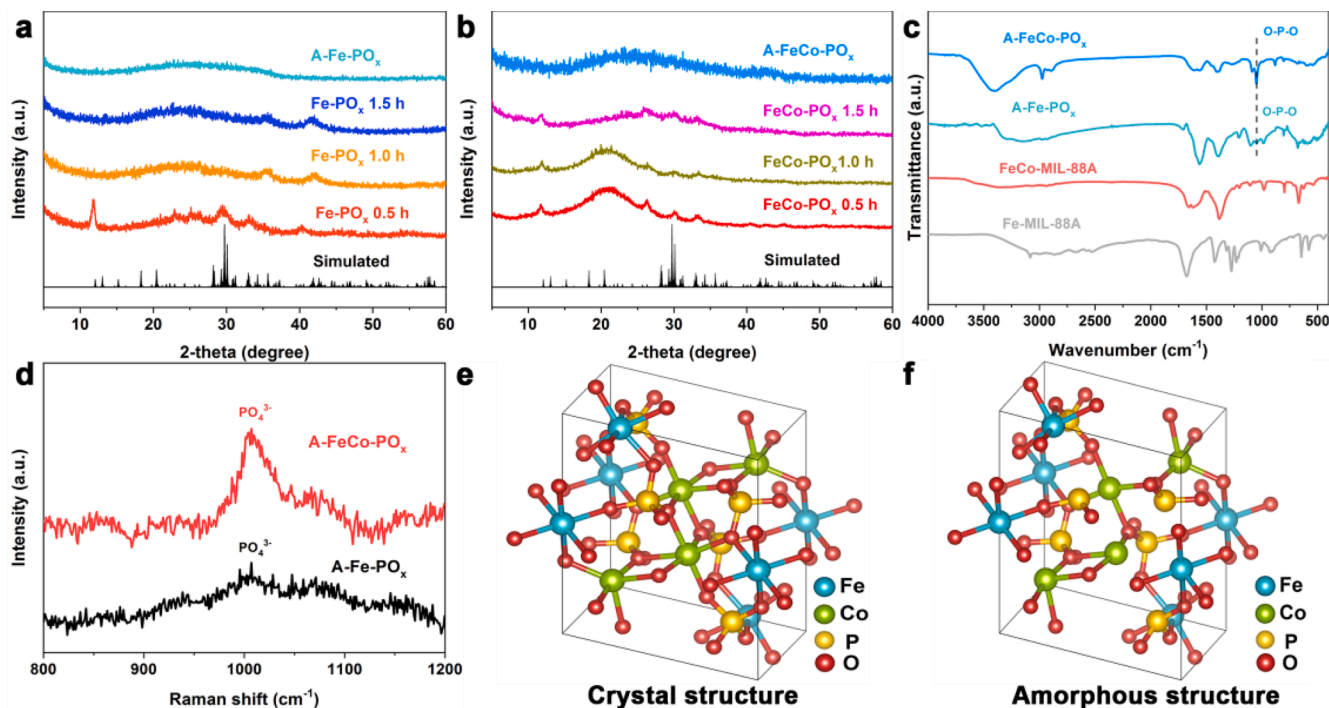


Fig. 2. (a) XRD patterns of Fe-PO_x 0.5 ~ 1.5 h and A-Fe-PO_x, (b) XRD patterns of FeCo-PO_x 0.5 ~ 1.5 h and A-FeCo-PO_x, (c) FT-IR spectra of fumaric acid, Fe-MIL-88A, FeCo-MIL-88A, A-Fe-PO_x and A-FeCo-PO_x, (d) Raman spectra of A-Fe-PO_x and A-FeCo-PO_x, and the possible atomic arrangements of (e) order structure and (f) disorder structure for A-FeCo-PO_x.

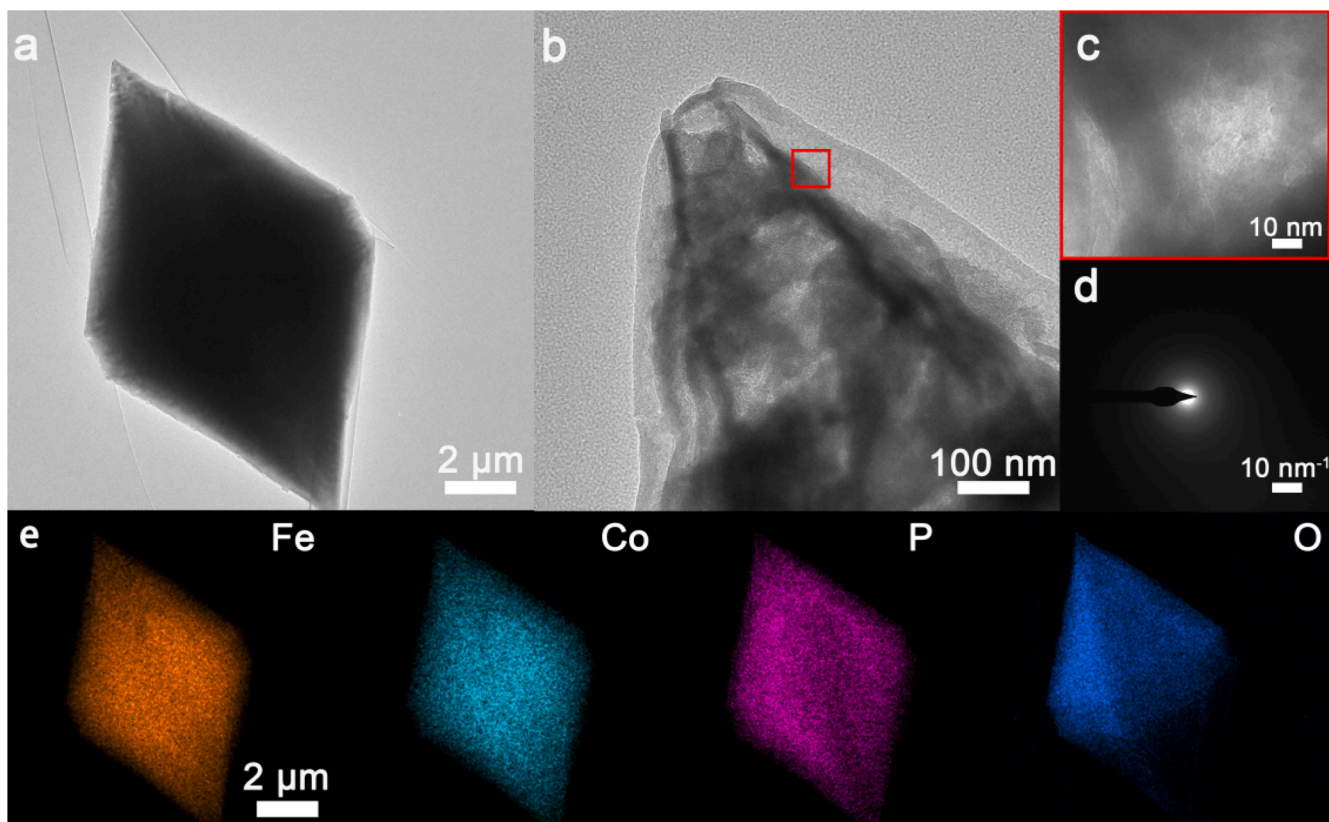


Fig. 3. (a–b) TEM images, (c) HR-TEM image, (d) SAED image, and (e) corresponding EDX elemental mappings of A-FeCo-PO_x.

composition of synthesized samples. As depicted in Fig. S7, the full survey spectrum of A-FeCo-PO_x indicated the presence of Fe, Co, P, and O elements, which aligned with the EDX results. The high-resolution Fe

2p spectrum in Fig. 4a displayed several deconvoluted peaks. The peak at 710.2 eV was attributed to Fe²⁺ 2p_{3/2}, while the second peak at 712.6 eV corresponded to the Fe³⁺ 2p_{3/2} components [49,50]. Additionally, a

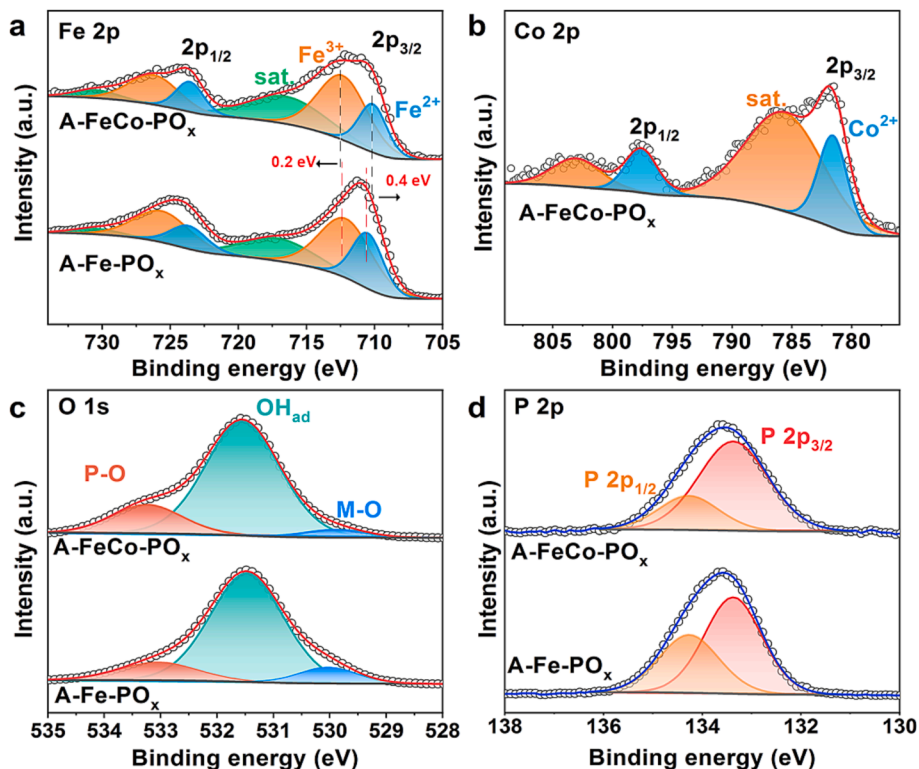


Fig. 4. XPS high-resolution spectra of (a) Fe 2p, (b) Co 2p, (c) O 1s and (d) P 2p for A-Fe-PO_x and A-FeCo-PO_x.

peak at 717.1 eV was deduced from a satellite peak. Interestingly, the $\text{Fe}^{2+} 2p_{3/2}$ peak of A-FeCo- PO_x was shifted to lower binding energy compared to A- Fe-PO_x , while the $\text{Fe}^{3+} 2p_{3/2}$ was shifted to higher binding energy, indicating that the bimetallic synergistic effect in A-FeCo- PO_x might affect the OER catalytic performance [51]. In the Co 2p XPS spectrum (Fig. 4b), four peaks were observed at 781.7 eV ($\text{Co}^{2+} 2p_{3/2}$), 797.6 eV ($\text{Co}^{2+} 2p_{1/2}$), and satellite peaks at 786.0 and 803.2 eV [52]. The O 1s spectra of A- Fe-PO_x and A-FeCo- PO_x were deconvoluted into three peaks at 529.8, 531.5, and 533.2 eV, which were assigned to M–O, OH species adsorbed on oxygen vacancy sites [53], and P–O, respectively [36] (Fig. 4c). As displayed in Fig. 4d, the P 2p spectrum was fitted into two peaks at 134.3 and 133.4 eV, corresponding to P $2p_{3/2}$ and P $2p_{1/2}$ of P–O bonds from the phosphate group [42].

3.2. Electrocatalytic performance

The electrocatalytic OER activity of synthesized samples was evaluated using a three-electrode setup in 1.0 M KOH. LSV was conducted at a scan rate of 5 mV s^{-1} and the data were corrected by 95% iR compensation to eliminate the influence of ohmic potential drop. The OER polarization curves of all samples were displayed in Fig. 5a. The improved OER activity of A-FeCo- PO_x compared to single A- Fe-PO_x and other contrast samples suggested that abundant oxygen vacancies and bimetallic synergistic effect contributed to better performance. Specifically, the overpotentials of A-FeCo- PO_x , FeCo- PO_x 1.5 h, FeCo- PO_x 1.0 h, FeCo- PO_x 0.5 h, and A- Fe-PO_x were 270, 287, 291, 292, and 342 mV, respectively, at a current density of 10 mA cm^{-2} . Moreover, A-FeCo- PO_x demonstrated a low Tafel slope of 39.5 mV dec^{-1} (Fig. 5b), which was lower than that of FeCo- PO_x 1.5 h (45.5 mV dec^{-1}), FeCo- PO_x 1.0 h (48.9 mV dec^{-1}), FeCo- PO_x 0.5 h (52.8 mV dec^{-1}), and A- Fe-PO_x (62.2 mV dec^{-1}), implying the fast OER reaction kinetics of A-FeCo- PO_x . Besides, the OER performance of A-FeCo- PO_x at different Fe/Co ratios was also compared. Fig. S8 indicated that the A-FeCo- PO_x exhibited peak OER performance at a Fe/Co feeding ratio of 2:1. In addition, the OER activity of A-FeCo- PO_x also exhibited reasonably good OER activity among the recently reported OER electrocatalysts (Fig. 5c and Table S2). To further evaluate the charge transfer kinetics, EIS measurements were performed. As shown in Fig. S9, A-FeCo- PO_x had the lowest charge

transfer resistance (R_{ct}) among the tested catalysts. The enhanced kinetics of A-FeCo- PO_x was attributed to the disordered atomic arrangement in the amorphous structure and synergistic effects between Fe and Co ions.

The turnover frequency (TOF) was used as a quantitative parameter to evaluate the intrinsic activity of samples, considering all metal centers of catalysts as active sites in an electrochemical process [54]. The calculated results of samples exhibited a volcanic trend in the following order: A-FeCo- $\text{PO}_x > \text{FeCo-PO}_x$ 1.5 h $> \text{FeCo-PO}_x$ 1.0 h $> \text{FeCo-PO}_x$ 0.5 h $> \text{A-Fe-PO}_x$ (Fig. 5d).

The electrochemically active surface area (ECSA) of samples was determined based on the double-layer capacitance (C_{dl}) within a non-Faradaic range of cyclic voltammograms (CV) curves obtained at an increasing scan rates to further account for the intrinsic OER activity (Fig. S10) [49]. As displayed in Fig. 5e, A-FeCo- PO_x had the highest C_{dl} (2.57 mF cm^{-2}) compared to FeCo- PO_x 1.5 h (2.30 mF cm^{-2}), FeCo- PO_x 1.0 h (1.49 mF cm^{-2}), FeCo- PO_x 0.5 h (1.45 mF cm^{-2}), and A- Fe-PO_x (1.42 mF cm^{-2}). A larger ECSA was beneficial for the exposure of more available active sites, facilitating electron transfer and enhancing OER electrochemical activity. The durability of A-FeCo- PO_x in OER was evaluated through CP tests in 1.0 M KOH at a current density of 10 mA cm^{-2} for 100 h (Fig. 5f). The change in potential was almost negligible, indicating the long-term solid stability of A-FeCo- PO_x . Additionally, a very negligible decay of OER activity was observed after 2400 continuous CV cycles, which further demonstrated the stability of A-FeCo- PO_x towards OER (inset: Fig. 5f).

To further validate the OER activity, diamond-like A-FeCo- PO_x was incorporated into the anode of overall water splitting (OWS) system and tested in 1.0 M KOH electrolyte (Fig. 6a). As shown in Fig. 6b, this OWS system required a cell voltage of 1.51 V at 10 mA cm^{-2} . Moreover, the cell voltage of A-FeCo- $\text{PO}_x^{(+)} || \text{Pt/C}^{(-)}$ OWS system exhibited better than that of recently reported two-electrode devices at 10 mA cm^{-2} (Fig. 6c, Table S3). The OWS system was operated at 200 mA cm^{-2} for 300 h with a voltage loss of only 9.1%, demonstrating the long-term solid stability of the A-FeCo- PO_x catalyst (Fig. 6d). These results confirmed that A-FeCo- PO_x was a novel practical electrocatalyst for OER in alkaline media.

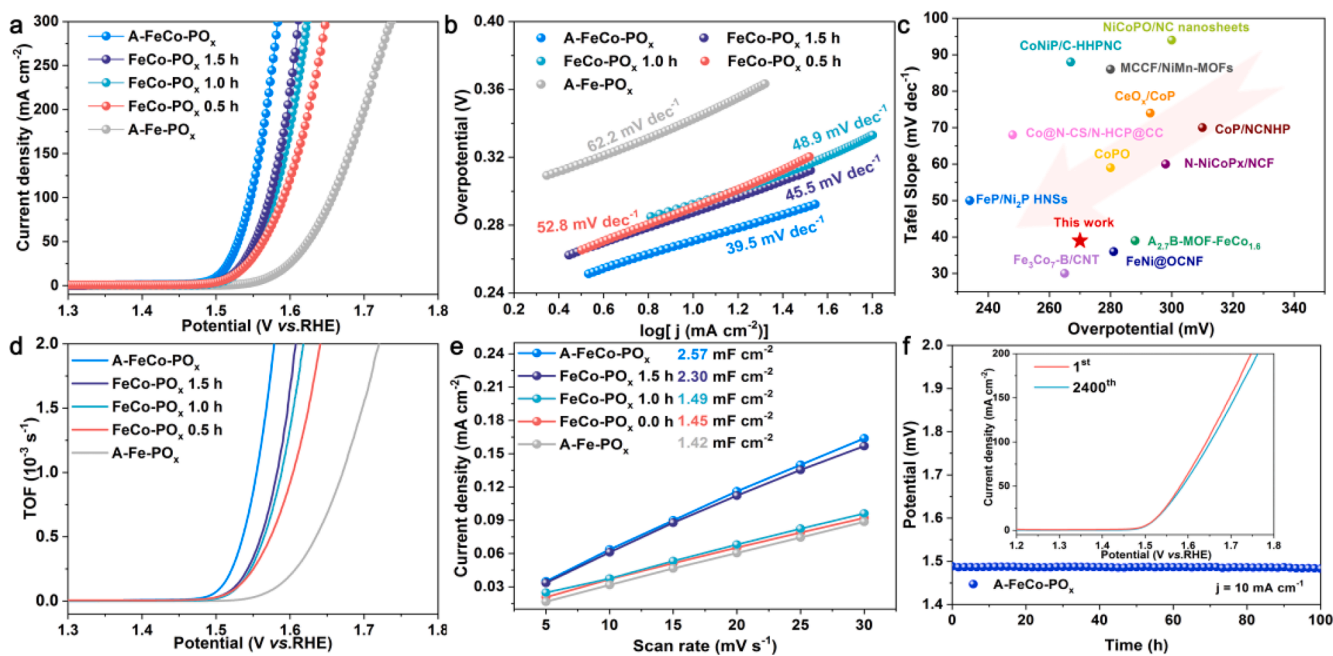


Fig. 5. OER performance of different catalysts in 1.0 M KOH. (a) LSV curves with iR -compensation, (b) Tafel plots, (c) overpotentials at 10 mA cm^{-2} and corresponding Tafel slopes of some previously reported catalysts, (d) the calculated TOF profiles, (e) the estimated C_{dl} values, and (f) chronopotentiometric curves of the long-term stability of electrodes at a constant current density of 10 mA cm^{-2} without iR compensation (Inset: polarization curves initial and after 2400 CV).

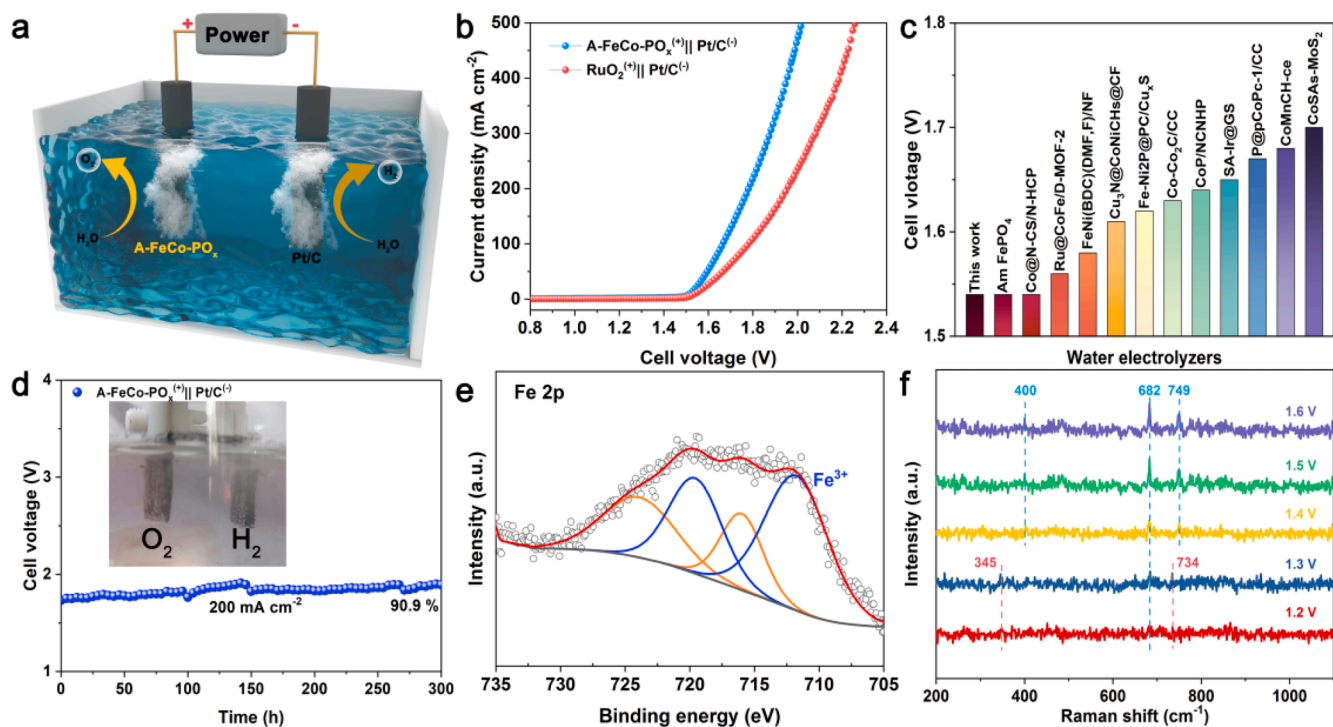


Fig. 6. (a) Schematic diagram of overall water splitting system. (b) Polarization curves of A-FeCo-PO_x⁽⁺⁾ || Pt/C⁽⁻⁾ and in 1.0 M KOH electrolyte. (c) Comparison of the alkaline OWS activity with previous reports at 10 mA cm⁻². (d) Chronopotentiometry test at 200 mA cm⁻². (e) XPS spectrum of Fe 2p for A-FeCo-PO_x after stability test. (f) In-situ Raman spectra of A-FeCo-PO_x electrode at different potential ranges (V vs. RHE) in 1.0 M KOH.

3.3. Catalytic mechanism analysis

The morphological and compositional changes of A-FeCo-PO_x after OER stability test were evaluated by XRD, SEM, and XPS. The XRD pattern in Fig. S11 revealed only the Bragg peaks of CFP, which suggested that the sample retained its characteristic amorphous features after OER stability test. Additionally, Fig. S12 showed that there were minimal alterations on the morphology of A-FeCo-PO_x after stability evaluation. Furthermore, XPS spectra of A-FeCo-PO_x were measured to detect the evolution of surface structure and elemental states after stability test. The full XPS survey of A-FeCo-PO_x exhibited the presence of C, O, F, S, P, Fe, and Co elements after stability test (Fig. S13a). The presence of S and F elements could be attributed to the addition of the Nafion solution during OER test. In the Fe 2p spectrum (Fig. 6e), the peaks of Fe²⁺ disappeared and the remaining peaks could be attributed to Fe³⁺, indicating the formation of FeOOH during the electrochemical process [55]. The Co 2p spectra (Fig. S13b) also showed the presence of Co³⁺ in A-FeCo-PO_x after stability test, which could be attributed to the transformation of Co²⁺ into CoOOH during the stability test [54,56]. Fig. S13c displayed a distinct P—O peak, albeit with reduced intensity. This suggested that PO_x remained within the internal structure. Moreover, the O 1s spectrum in Fig. S13d confirmed the emergence of oxyhydroxide on the surface during stability test. This observation was consistent with the results of the Fe 2p and Co 2p XPS spectra in the A-FeCo-PO_x post-stability assessment.

The reconstruction mechanism of A-FeCo-PO_x during the OER process was explored in 1.0 M KOH via in-situ Raman spectroscopy. At the potential of 1.2 V vs. RHE, the peaks near 682 and 734 cm⁻¹ could be associated with Fe-O vibrations, while the 345 cm⁻¹ peak corresponded to the Co-O vibration in Co(OH)₂ (Fig. 6f) [57–59]. As potential increased, the characteristic peaks of A-FeCo-PO_x began to disappear and were replaced by characteristic peaks of the metal-oxyhydroxides, indicating that a phase change occurred during the OER process [60]. Interestingly, the peaks at 345 and 734 cm⁻¹ were blueshifted as the potential rose to 1.4 V vs. RHE. The peaks at 400 and 749 cm⁻¹ were

consistent with CoOOH and FeOOH, suggesting a transition from hydroxide to oxyhydroxide [61]. These results suggested that A-FeCo-PO_x underwent surface reconstruction during the OER process, and the in-situ generated metal oxyhydroxides were the real active species in the electrocatalytic reaction [54]. Based on above analysis and previous reports, the corresponding OER mechanism of A-FeCo-PO_x was shown in Fig. S14, in which Fe site was considered as adsorption site [18,49,59]. This mechanism consisted of adsorption structures of O*, OH*, and OOH* intermediates for each fundamental step. For A-FeCo-PO_x, all four foundational reactions in the OER sequence occurred at the Fe site of the surface oxyhydroxides.

The OER performance and stability of A-FeCo-PO_x can be attributed to several factors. (1) The problems of low conductivity and high overpotentials for pristine MOFs could be solved by doping P species with lower electronegativity. (2) The strong synergistic effect between the amorphous structure and the abundant oxygen vacancies modulates the electronic structure, thereby improving electronic/mass transport and reaction kinetics. (3) The synergistic reaction between the metal Fe and Co accelerates the adsorption/desorption process of OER intermediates.

4. Conclusion

In summary, we have firstly uncovered the influence of tunable crystallinity and oxygen vacancies in FeCo-PO_x on the optimization of high-current water splitting. The amorphous FeCo-PO_x with oxygen vacancies was synthesized from crystalline to amorphous states by deliberately tuning the anion etching process. The optimized A-FeCo-PO_x catalyst exhibited lower overpotential of 270 mV at 10 mA cm⁻² with a Tafel slope of 39 mV dec⁻¹ compared to CNS-rGO [32], FePB/NiFeP [34], a-NiFeMo [38] and CeO_x/Co-2-MIM [26]. Interestingly, overall water splitting system assembled with A-FeCo-PO_x⁽⁺⁾ || Pt/C⁽⁻⁾ displayed long-term solid durability, maintaining for 300 h at 200 mA cm⁻² with minimal degradation. The optimized OER performance is due to the combined effect of oxygen vacancies and the amorphous

structure, which accelerates electron transfer and lowers the OER energy barrier. A-FeCo-PO_x is optimized compared to traditional crystalline counterparts and RuO₂-based catalyst in terms of activity and endurance. In essence, the study in this paper might pave the way for synthesizing amorphous materials tailored for electrochemical water electrolysis, setting the stage for potential industrial applications in the near future.

CRedit authorship contribution statement

Xinqiang Liu: Investigation, Data curation, Writing – original draft. **Haoran Yin:** Validation, Formal analysis. **Shifan Zhang:** Investigation, Validation. **Menghan Huang:** Investigation, Validation. **Tayirjan Tayior Isimjan:** Writing – review & editing. **Xiulin Yang:** Supervision, Writing – review & editing. **Dandan Cai:** Supervision, Funding acquisition, Writing – review & editing.

Declaration of Competing Interest

The authors declare that they have no known competing financial interests or personal relationships that could have appeared to influence the work reported in this paper.

Data availability

No data was used for the research described in the article.

Acknowledgements

This work was financially supported by the National Natural Science Foundation of China (No. 22068008, 21965005, 52363028), Guangxi Province Natural Science Foundation (No. 2020GXNSFAA159104, 2019GXNSFGA245003).

Appendix A. Supplementary data

Supplementary data to this article can be found online at <https://doi.org/10.1016/j.jcis.2023.09.185>.

References

- H. Xie, Z. Zhao, T. Liu, Y. Wu, C. Lan, W. Jiang, L. Zhu, Y. Wang, D. Yang, Z. Shao, A membrane-based seawater electrolyser for hydrogen generation, *Nature* 612 (2022) 673–678, <https://doi.org/10.1038/s41586-022-05379-5>.
- X. Xu, H. Sun, S.P. Jiang, Z. Shao, Modulating metal–organic frameworks for catalyzing acidic oxygen evolution for proton exchange membrane water electrolysis, *SusMat* 1 (2021) 460–481, <https://doi.org/10.1002/sus2.34>.
- K. Wang, X. Wang, Z. Li, B. Yang, M. Ling, X. Gao, J. Lu, Q. Shi, L. Lei, G. Wu, Y. Hou, Designing 3d dual transition metal electrocatalysts for oxygen evolution reaction in alkaline electrolyte: beyond oxides, *Nano Energy* 77 (2020), 105162, <https://doi.org/10.1016/j.nanoen.2020.105162>.
- C. Zhang, F. Wang, M. Batool, B. Xiong, H. Yang, Phase transition of SrCo_{0.9}Fe_{0.1}O₃ electrocatalysts and their effects on oxygen evolution reaction, *SusMat* 2 (2022) 445–455, <https://doi.org/10.1002/sus2.72>.
- G. Righi, J. Plescher, F.-P. Schmidt, R.K. Campen, S. Fabris, A. Knop-Gericke, R. Schlögl, T.E. Jones, D. Teschner, S. Piccinin, On the origin of multihole oxygen evolution in haematite photoanodes, *Nat. Catal.* 5 (2022) 888–899, <https://doi.org/10.1038/s41929-022-00845-9>.
- J. Song, C. Wei, Z.-F. Huang, C. Liu, L. Zeng, X. Wang, Z.J. Xu, A review on fundamentals for designing oxygen evolution electrocatalysts, *Chem. Soc. Rev.* 49 (2020) 2196–2214, <https://doi.org/10.1039/C9CS00607A>.
- S. Li, Y. Gao, N. Li, L. Ge, X. Bu, P. Feng, Transition metal-based bimetallic MOFs and MOF-derived catalysts for electrochemical oxygen evolution reaction, *Energ. Environ. Sci.* 14 (2021) 1897–1927, <https://doi.org/10.1039/D0EE03697H>.
- K. Zhang, R. Zou, Advanced transition metal-based OER electrocatalysts: current status, Opportunities Challenges *Small* 17 (2021) 2100129, <https://doi.org/10.1002/smll.202100129>.
- C. Hu, Q. Liang, Y. Yang, Q. Peng, Z. Luo, J. Dong, T.T. Isimjan, X. Yang, Conductivity-enhanced porous n/p co-doped metal-free carbon significantly enhances oxygen reduction kinetics for aqueous/flexible zinc-air batteries, *J. Colloid Interface Sci.* 633 (2023) 500–510, <https://doi.org/10.1016/j.jcis.2022.11.118>.
- J. Joy, S. Rajappa, V.K. Pillai, S. Alwarappan, Co₃Fe₇/nitrogen-doped graphene nanoribbons as bi-functional electrocatalyst for oxygen reduction and oxygen evolution, *Nanotechnol.* 29 (2018), 415402, <https://doi.org/10.1088/1361-6528/aad35e>.
- J. Joy, A. Sekar, S. Vijayaraghavan, P. Kumar T, V.K. Pillai, S. Alwarappan, Nickel-Incorporated, Nitrogen-Doped Graphene Nanoribbons as Efficient Electrocatalysts for Oxygen Evolution Reaction, *J. Electrochem. Soc.* 165 (2018), H141, <https://dx.doi.org/10.1149/2.0601803jes>.
- T.V. Vineesh, S. Mubarak, M.G. Hahm, V. Prabu, S. Alwarappan, T.N. Narayanan, Controllably alloyed, low density, free-standing Ni-Co and Ni-Graphene sponges for electrocatalytic water splitting, *Sci. Rep.* 6 (2016) 31202, <https://doi.org/10.1038/srep31202>.
- R.K. Joshi, S. Shukla, S. Saxena, G.H. Lee, V. Sahajwalla, S. Alwarappan, Hydrogen generation via photoelectrochemical water splitting using chemically exfoliated MoS₂ layers, *AIP Adv.* 6 (2016), 015315, <https://doi.org/10.1063/1.4941062>.
- T.V. Vineesh, M.P. Kumar, C. Takahashi, G. Kalita, S. Alwarappan, D. K. Pattanayak, T.N. Narayanan, Bifunctional electrocatalytic activity of boron-doped graphene derived from boron carbide, *Adv. Energy Mater.* 5 (2015) 1500658, <https://doi.org/10.1002/aenm.201500658>.
- L.-M. Cao, J. Zhang, L.-W. Ding, Z.-Y. Du, C.-T. He, metal-organic frameworks derived transition metal phosphides for electrocatalytic water splitting, *J. Energy Chem.* 68 (2022) 494–520, <https://doi.org/10.1016/j.jechem.2021.12.006>.
- Z. Luo, Q. Peng, Z. Huang, L. Wang, Y. Yang, J. Dong, T.T. Isimjan, X. Yang, Fine-tune d-band center of cobalt vanadium oxide nanosheets by n-doping as a robust overall water splitting electrocatalyst, *J. Colloid Interface Sci.* 629 (2023) 111–120, <https://doi.org/10.1016/j.jcis.2022.09.069>.
- W. Kang, R. Wei, H. Yin, D. Li, Z. Chen, Q. Huang, P. Zhang, H. Jing, X. Wang, C. Li, Unraveling sequential oxidation kinetics and determining roles of multi-cobalt active sites on Co₃O₄ catalyst for water oxidation, *J. Am. Chem. Soc.* 145 (2023) 3470–3477, <https://doi.org/10.1021/jacs.2c11508>.
- D. Friebe, M.W. Louie, M. Bajdich, K.E. Sanwald, Y. Cai, A.M. Wise, M.-J. Cheng, D. Sokaras, T.-C. Weng, R. Alonso-Mori, R.C. Davis, J.R. Bargar, J.K. Nørskov, A. Nilsson, A.T. Bell, Identification of highly active Fe sites in (Ni, Fe)OOH for electrocatalytic water splitting, *J. Am. Chem. Soc.* 137 (2015) 1305–1313, <https://doi.org/10.1021/ja511559d>.
- W. Cheng, X. Zhao, H. Su, F. Tang, W. Che, H. Zhang, Q. Liu, Lattice-strained metal–organic-framework arrays for bifunctional oxygen electrocatalysis, *Nat. Energy* 4 (2019) 115–122, <https://doi.org/10.1038/s41560-018-0308-8>.
- Y. Shi, B. Zhang, Correction: Recent advances in transition metal phosphide nanomaterials: synthesis and applications in hydrogen evolution reaction, *Chem. Soc. Rev.* 45 (2016) 1781, <https://doi.org/10.1039/C6CS90013E>.
- L. Wang, H. Yu, Z. Huang, Z. Luo, T.T. Isimjan, S. Xu, X. Yang, Interface engineering of porous nickel-iron phosphates with enriched oxygen vacancies as an efficient bifunctional electrocatalyst for high current water splitting, *Electrochim. Acta* 443 (2023) 141932, <https://doi.org/10.1016/j.electacta.2023.141932>.
- Y. Li, Z. Dong, L. Jiao, Multifunctional transition metal-based phosphides in energy-related electrocatalysis, *Adv. Energy Mater.* 10 (2020) 1902104, <https://doi.org/10.1002/aenm.201902104>.
- J. Shi, F. Qiu, W. Yuan, M. Guo, Z.-H. Lu, Nitrogen-doped carbon-decorated yolk-shell CoP@FeCoP micro-polyhedra derived from MOF for efficient overall water splitting, *Chem. Eng. J.* 403 (2021), 126312, <https://doi.org/10.1016/j.cej.2020.126312>.
- Y. Wang, Y. Wang, H. Gao, Z. Huang, Q. Hao, B. Liu, Interface-induced contraction of core–shell prussian blue analogues toward hollow Ni-Co-Fe phosphide nanoboxes for efficient oxygen evolution electrocatalysis, *Chem. Eng. J.* 451 (2023) 138515, <https://doi.org/10.1016/j.cej.2022.138515>.
- Q. Qian, Y. Li, Y. Liu, G. Zhang, General anion-exchange reaction derived amorphous mixed-metal oxides hollow nanoprisms for highly efficient water oxidation electrocatalysis, *Appl. Catal. B Environ.* 266 (2020) 118642, <https://doi.org/10.1016/j.apcatb.2020.118642>.
- X. Wu, J. Wei, T. Zhang, Y. Yang, Q. Liu, X. Yan, Y. Tang, Novel synthesis of in situ CeO_x nanoparticles decorated on CoP nanosheets for highly efficient electrocatalytic oxygen evolution, *Inorg. Chem. Front.* 8 (2021) 4440–4447, <https://doi.org/10.1039/D1QI00821H>.
- J. Liu, L. Guo, In situ self-reconstruction inducing amorphous species: A key to electrocatalysis, *Matter* 4 (2021) 2850–2873, <https://doi.org/10.1016/j.matt.2021.05.025>.
- Y. Zhou, H.J. Fan, Progress and challenge of amorphous catalysts for electrochemical water splitting, *ACS Mater. Lett.* 3 (2021) 136–147, <https://doi.org/10.1021/acsmaterialslett.0c00502>.
- Y. Xu, K. Ren, R. Xu, In situ formation of amorphous Fe-based bimetallic hydroxides from metal-organic frameworks as efficient oxygen evolution catalysts, *Chinese J. Catal.* 42 (2021) 1370–1378, [https://doi.org/10.1016/S1872-2067\(20\)63741-X](https://doi.org/10.1016/S1872-2067(20)63741-X).
- X. Zhang, G. Li, Y. Zhang, D. Luo, A. Yu, X. Wang, Z. Chen, Amorphizing metal-organic framework towards multifunctional polysulfide barrier for high-performance lithium-sulfur batteries, *Nano Energy* 86 (2021) 106094, <https://doi.org/10.1016/j.nanoen.2021.106094>.
- J. Ding, T. Fan, K. Shen, Y. Li, Electrochemical synthesis of amorphous metal hydroxide microarrays with rich defects from MOFs for efficient electrocatalytic water oxidation, *Appl. Catal. B Environ.* 292 (2021) 120174, <https://doi.org/10.1016/j.apcatb.2021.120174>.
- Y.-R. Hong, S. Mhin, K.-M. Kim, W.-S. Han, H. Choi, G. Ali, K.Y. Chung, H.J. Lee, S.-I. Moon, S. Dutta, S. Sun, Y.-G. Jung, T. Song, H. Han, Electrochemically activated cobalt nickel sulfide for an efficient oxygen evolution reaction: partial amorphization and phase control, *J. Mater. Chem. A* 7 (2019) 3592–3602, <https://doi.org/10.1039/C8TA10142F>.

- [33] J. Han, J. Zhang, T. Wang, Q. Xiong, W. Wang, L. Cao, B. Dong, Zn doped FeCo layered double hydroxide nanoneedle arrays with partial amorphous phase for efficient oxygen evolution reaction, *ACS Sustain. Chem. Eng.* 7 (2019) 13105–13114, <https://doi.org/10.1021/acsschemeng.9b02297>.
- [34] X. Zhang, Y. Li, Z. Wu, H. Sheng, Y. Hu, C. Li, H. Li, L. Cao, B. Dong, Crystalline/amorphous composite interface induced by NaBH₄ hydrolysis reaction: a new interfacial electrocatalyst for efficient oxygen evolution reaction, *Mater. Today Energy* 26 (2022) 100987, <https://doi.org/10.1016/j.mtener.2022.100987>.
- [35] S. Anantharaj, S. Noda, Amorphous catalysts and electrochemical water splitting: An untold story of harmony, *Small* 16 (2020) 1905779, <https://doi.org/10.1002/smll.201905779>.
- [36] L. Zhang, H. Jang, H. Liu, M.G. Kim, D. Yang, S. Liu, X. Liu, J. Cho, Sodium-decorated amorphous/crystalline RuO₂ with rich oxygen vacancies: a robust pH-universal oxygen evolution electrocatalyst, *Angew. Chem. Int. Ed.* 60 (2021) 18821–18829, <https://doi.org/10.1002/anie.202106631>.
- [37] W. Xu, H. Wang, Earth-abundant amorphous catalysts for electrolysis of water, *Chinese J. Catal.* 38 (2017) 991–1005, [https://doi.org/10.1016/S1872-2067\(17\)62810-9](https://doi.org/10.1016/S1872-2067(17)62810-9).
- [38] Y. Duan, Z.-Y. Yu, S.-J. Hu, X.-S. Zheng, C.-T. Zhang, H.-H. Ding, B.-C. Hu, Q.-Q. Fu, Z.-L. Yu, X. Zheng, J.-F. Zhu, M.-R. Gao, S.-H. Yu, Scaled-Up synthesis of amorphous NiFeMo oxides and their rapid surface reconstruction for superior oxygen evolution catalysis, *Angew. Chem. Int. Ed.* 58 (2019) 15772–15777, <https://doi.org/10.1002/anie.201909939>.
- [39] G. Wu, X. Zheng, P. Cui, H. Jiang, X. Wang, Y. Qu, W. Chen, Y. Lin, H. Li, X. Han, Y. Hu, P. Liu, Q. Zhang, J. Ge, Y. Yao, R. Sun, Y. Wu, L. Gu, X. Hong, Y. Li, A general synthesis approach for amorphous noble metal nanosheets, *Nat. Commun.* 10 (2019) 4855, <https://doi.org/10.1038/s41467-019-12859-2>.
- [40] T.D. Bennett, A.K. Cheetham, Amorphous metal-organic frameworks, *Acc. Chem. Res.* 47 (2014) 1555–1562, <https://doi.org/10.1021/ar5000314>.
- [41] C. Mellot-Draznieks, C. Serre, S. Surblé, N. Audebrand, G. Férey, Very large swelling in hybrid frameworks: a combined computational and powder diffraction study, *J. Am. Chem. Soc.* 127 (2005) 16273–16278, <https://doi.org/10.1021/ja054900x>.
- [42] M. Guo, M. Xu, Y. Qu, C. Hu, P. Yan, T.T. Isimjan, X. Yang, electronic/mass transport increased hollow porous Cu₃P/MoP nanospheres with strong electronic interaction for promoting oxygen reduction in Zn-air batteries, *Appl. Catal. B Environ.* 297 (2021) 120415, <https://doi.org/10.1016/j.apcatb.2021.120415>.
- [43] L. Wang, Y. Qin, H. Li, Z. Huang, M. Gao, T.T. Isimjan, X. Yang, oxygen vacancy engineering of mesoporous Bi-Fe₂O₃@NC multi-channel microspheres for remarkable oxygen reduction and aqueous/flexible Zn-air batteries, *J. Colloid Interface Sci.* 650 (2023) 719–727, <https://doi.org/10.1016/j.jcis.2023.07.033>.
- [44] G. Cui, Y. Zeng, J. Wu, Y. Guo, X. Gu, X.W. Lou, Synthesis of nitrogen-doped KMnO₄ with oxygen vacancy for stable zinc-ion batteries, *Adv. Sci.* 9 (2022) 2106067, <https://doi.org/10.1002/adv.202106067>.
- [45] L.-Y. Duan, F.-C. Liu, E.-B. Wang, Y.-G. Li, C.-W. Hu, L. Xu, Hydrothermal synthesis and properties of open-framework mixed-valence iron phosphates Fe^{III}₂Fe^{II}_{1.5}(PO₄)₃ with three-dimensional structure, *Chinese J. Chem.* 22 (2004) 55–59, <https://doi.org/10.1002/cjoc.20040220113>.
- [46] Y. Qian, S. Jiang, Y. Li, Z. Yi, J. Zhou, T. Li, Y. Han, Y. Wang, J. Tian, N. Lin, Y. Qian, in situ revealing the electroactivity of p–O and p–C bonds in hard carbon for high-capacity and long-life Li/K-ion batteries, *Adv. Energy Mater.* 9 (2019) 1901676, <https://doi.org/10.1002/aenm.201901676>.
- [47] H. Feng, J. Yu, L. Tang, J. Wang, H. Dong, T. Ni, J. Tang, W. Tang, X. Zhu, C. Liang, Improved hydrogen evolution activity of layered double hydroxide by optimizing the electronic structure, *Appl. Catal. B Environ.* 297 (2021) 120478, <https://doi.org/10.1016/j.apcatb.2021.120478>.
- [48] S. Wen, X. Gu, X. Ding, P. Dai, D. Zhang, L. Li, D. Liu, X. Zhao, J. Yang, Boosting fast and stable alkali metal ion storage by synergistic engineering of oxygen vacancy and amorphous structure, *Adv. Funct. Mater.* 32 (2022) 2106751, <https://doi.org/10.1002/adfm.202106751>.
- [49] F. Li, Y. Tian, S. Su, C. Wang, D.-S. Li, D. Cai, S. Zhang, Theoretical and experimental exploration of tri-metallic organic frameworks (t-MOFs) for efficient electrocatalytic oxygen evolution reaction, *Appl. Catal. B Environ.* 299 (2021) 120665, <https://doi.org/10.1016/j.apcatb.2021.120665>.
- [50] Z. Wan, D. Yang, J. Chen, J. Tian, T.T. Isimjan, X. Yang, Oxygen-evolution catalysts based on iron-mediated nickel metal-organic frameworks, *ACS Appl. Nano Mater.* 2 (2019) 6334–6342, <https://doi.org/10.1021/acsnm.9b01330>.
- [51] X. Hou, Z. Han, X. Xu, D. Sarker, J. Zhou, M. Wu, Z. Liu, M. Huang, H. Jiang, Controllable amorphization engineering on bimetallic metal-organic frameworks for ultrafast oxygen evolution reaction, *Chem. Eng. J.* 418 (2021) 129330, <https://doi.org/10.1016/j.cej.2021.129330>.
- [52] Z. Xue, K. Liu, Q. Liu, Y. Li, M. Li, C.Y. Su, N. Ogiwara, H. Kobayashi, H. Kitagawa, M. Liu, G. Li, Missing-linker metal-organic frameworks for oxygen evolution reaction, *Nat. Commun.* 10 (2019) 5048, <https://doi.org/10.1038/s41467-019-13051-2>.
- [53] H. Idriss, On the wrong assignment of the XPS O1s signal at 531–532 eV attributed to oxygen vacancies in photo- and electro-catalysts for water splitting and other materials applications, *Surf. Sci.* 712 (2021) 121894, <https://doi.org/10.1016/j.susc.2021.121894>.
- [54] S. Zhao, C. Tan, C.-T. He, P. An, F. Xie, S. Jiang, Y. Zhu, K.-H. Wu, B. Zhang, H. Li, J. Zhang, Y. Chen, S. Liu, J. Dong, Z. Tang, Structural transformation of highly active metal-organic framework electrocatalysts during the oxygen evolution reaction, *Nat. Energy* 5 (2020) 881–890, <https://doi.org/10.1038/s41560-020-00709-1>.
- [55] S.Y. Lim, S. Park, S.W. Im, H. Ha, H. Seo, K.T. Nam, Chemically deposited amorphous Zn-doped NiFeO_xH_y for enhanced water oxidation, *ACS Catal.* 10 (2020) 235–244, <https://doi.org/10.1021/acscatal.9b03544>.
- [56] G. Zhang, Z. Li, J. Zeng, L. Yu, C. Zuo, P. Wen, Y. Liu, L. Zhong, H. Chen, Y. Qiu, Ferric ions leached from Fe-based catalyst to trigger the dynamic surface reconstruction of nickel foam for high-efficient OER activity, *Appl. Catal. B Environ.* 319 (2022) 121921, <https://doi.org/10.1016/j.apcatb.2022.121921>.
- [57] W. Chen, Y. Xie, X. Gao, L. Li, Z. Lin, Simultaneous optimization of CoIr alloy nanoparticles and 2D graphitic-N doped carbon support in CoIr@CN by ir doping for enhanced oxygen and hydrogen evolution reactions, *J. Mater. Chem. A* 10 (2022) 15543–15553, <https://doi.org/10.1039/D2TA03496D>.
- [58] R. S, N.G.K. D, U.K. Mudali, In-situ Raman and X-ray photoelectron spectroscopic studies on the pitting corrosion of modified 9Cr-1Mo steel in neutral chloride solution, *Appl. Surf. Sci.* 428 (2018), 1106–1118, <https://doi.org/10.1016/j.apsusc.2017.09.179>.
- [59] B.M. Kathale, H. Xiao, S. Yang, H. Yin, T. Yu, X. Zhou, L. Qian, J. Xiao, P. Lei, X. Li, Fluoride mediated conversion of Fe(OH) into NiFe(OOH) for outstanding oxygen evolution reaction, *Electrochim. Acta* 406 (2022) 139831, <https://doi.org/10.1016/j.electacta.2022.139831>.
- [60] K. Fan, H. Zou, Y. Lu, H. Chen, F. Li, J. Liu, L. Sun, L. Tong, M.F. Toney, M. Sui, J. Yu, Direct observation of structural evolution of metal chalcogenide in electrocatalytic water oxidation, *ACS Nano* 12 (2018) 12369–12379, <https://doi.org/10.1021/acsnano.8b06312>.
- [61] Q. Li, Q. Chen, S. Lei, M. Zhai, G. Lv, M. Cheng, L. Xu, H. Xu, Y. Deng, J. Bao, Crystalline Ni-Fe phosphide/amorphous P doped Fe-(oxy)hydroxide heterostructure as a multifunctional electrocatalyst for solar cell-driven hydrogen production, *J. Colloid Interface Sci.* 631 (2023) 56–65, <https://doi.org/10.1016/j.jcis.2022.10.130>.